Journal of Fluids and Structures 128 (2024) 104138

Contents lists available at ScienceDirect

Journal of Fluids and Structures

journal homepage: www.elsevier.com/locate/jfs

Vortex dynamics in the wake of bio-inspired flexible, slotted winglets

Alden Midmer *, Christoph Brücker

City, University of London, Northampton Square 10, EC1V0HB London, UK

ARTICLE INFO

Keywords:
Slotted wingtip
Bio-inspired
PIV
Vortex
Self-adaptive

ABSTRACT

Flexible wingtip extensions matched to the Cauchy and Reynolds numbers of a peregrine falcon's primary feather in flight have been tested in differing configurations and compared to rigid ones for reference. The wingtip configurations were attached to the end of a symmetric (NACA 0012) aerofoil and were tested at 5° and 10° angles of attack and Reynolds numbers of 70k and 90k. Time resolved particle image velocimetry (TR-PIV) was used to study the dynamics of the individual vortices. The results show that, at increased angle of attack the configuration with C-type variation of the free length of the winglets is spreading the vorticity into spanwise and vertical directions, generating a circular multi-core vortex arrangement. In contrast, for the case of winglets of the same length (I-type configuration) a continuous vortex sheet is formed which rolls up into a single core, dislocated outboards and upwards from the original tip-vortex location. This remains the case even for larger angle of attack. It is concluded that – besides the known reduction of induced drag – the former configuration is also beneficial for a more rapid disintegration of the tip-vortex in the wake, while the latter shows less instability. This let us speculate that the latter could be relevant for reducing the tip-noise at higher angle of attack such as for Owls, who hunt during night and have adapted to fly silently.

1. Introduction

Bio-inspired winglets have become an increasingly popular area of research with the promise of improved aerodynamic performance. None more so than the mimicking of cascading or multi-wingtips that are most commonly found in thermal soaring, high wing loading birds (Liu et al., 2021). And the alternative, pointed wingtips, is commonly found on dynamic soaring birds such as the Albatross which are perfected for soaring flight. The two types of wingtips are optimised for different flight conditions with the multi-wingtips being more suited to high lift phases and the pointed wingtip for cruising; thus it can be inferred an ideal wingtip will be able to adapt between the two.

Within the subsection of slotted wingtips slight differences can be identified, as shown in 1. The Barn owl, optimised for quiet nocturnal flight, has a more rounded wingtip and feather tips that are inline with other. Whereas the Turkey vulture, optimised for thermal soaring, has longer tip feathers which are more spatially separated in all planes. But, of particular interest to this study is the peregrine falcon which displays a cascading, slotted, wingtip during high angles of attack (such as during landing) and a pointed wingtip with the feathers together during cruise. A similar observation can be seen on the black vulture, where the wing and wingtip are adapted between soaring and gliding flight. During gliding the vulture's wing is retracted, reducing the span and consequently shielding the tip feathers from the airflow. But, in soaring flight the wingtip feathers are spread and exposed to the flow, reducing induced drag at the expense of increased profile drag (Newman, 1958).

* Corresponding author.
E-mail address: alden.midmer@city.ac.uk (A. Midmer).

https://doi.org/10.1016/j.jfluidstructs.2024.104138
Received 30 September 2023; Received in revised form 17 May 2024; Accepted 20 May 2024

(a) Barn owl in flight by Servant 2013 (CC BY 2.0 (https://creativecommons.org/licenses/by/2.0))

(b) Turkey vulture in flight by Sharp (2016) (CC BY-SA 4.0 (https://creativecommons.org/licenses/by-sa/4.0/deed.en/)).

Fig. 1. Examples of slotted wingtips observed in nature (see Servant, 2013; Sharp, 2016).

Multiple studies on live birds and using real feathers to determine the benefits of a slotted wingtip have been conducted. This includes testing on a live jackdaw in flapping and gliding flight, demonstrating the spreading of vorticity by the cascaded wingtip feathers (KleinHeerenbrink et al., 2017). This was found to improve span efficiency by up to 6.6% when compared to an optimal planar wing. Other experimental studies used a base wing with a feathered extension (Tucker, 1993), which concluded a slotted wingtip could have a drag reduction of 12% when compared to a planar wing. Following, a study on a live Harris hawk with unclipped and clipped wingtip feathers came to the same conclusion that slotted wingtips reduce induced drag by the spreading of the vortex sheet (Tucker, 1995).

Further experimental and theoretical studies have inspiration or mimicking of various aspects of slotted wingtips, ranging from dihedral (Liu et al., 2023) to extension inter-spacing (Lynch et al., 2018). The effects of slots, specifically on a stork's wingtip, have also been modelled and studied numerically and have also shown to break up the singular vortex (Tangermann et al., 2022). Other theoretical studies on static non-planar wingtips have found an improved aerodynamic efficiency, however the necessity to have an adaptive structure in order to maintain optimal wing loading (Cone, 1962). A more recent study on the effects of flexibility showed that a small increase in aerodynamic performance could gained with the use of flexible tips but a higher increase could be achieved with rigid tips (Siddiqui et al., 2018).

Other benefits of an adaptable feather-like surface have been demonstrated to be able to diminish wing loads in highly turbulent airflow conditions, see Wissa et al. (2015). In low turbulence conditions the feathers were latched together while in severe aerodynamic conditions such as gusts, the feathers separated and alleviated the load. In addition to the aerodynamic benefits, it is suggested (through studies on tip vortex development, Klei et al. (2014)) that nature-inspired wingtips may also have other advantages, such as reduced tip-vortex noise if they reduce the size of the vortex produced.

The present study builds off previous research in order to further explore the potential of flexible extensions on the wingtip and to fill the current gap in research on flexible slotted wingtips (Liu et al., 2021). Prior studies have already demonstrated the spreading of vorticity through mimicking avian slotted wingtips with flexible extensions (Midmer and Bruecker, 2022). However the effects of varying the extension lengths was not analysed, nor is it clear how an optimum vortex spreading configuration might look like for different flow conditions.

2. Flow tunnel and wing model

The aerofoil used was a NACA 0012, with a chord (c) of 300 mm. The typical avian flight is in the order of 10^5 Reynolds number which can easily be matched at relatively low velocities in a water tunnel. The tunnel is an open-surface water channel with a honeycomb mesh located upstream of the test section. The test section has dimensions of 0.4 m width, 0.5 m depth and 1.2 m length (see Fig. 2). In this study a Re-number of $Re = 70{,}000$ was chosen, resulting in a freestream velocity of $23.3\,\mathrm{cm\,s^{-1}}$.

The tip of the wing model has 5 slots, which contain 5 extensions made of plastic (length = $0.33c$, width = $0.07c$, thickness = $0.005c$, inter-spacing = $0.03c$). Housed within the aerofoil, situated behind each extension, were 5 pneumatic actuators with a control box that enabled the individual deployment of each extension from fully retracted to fully extended. Two different extension types were used, one which was flexible - used to mimic a peregrine falcon's primary feather - and the second was rigid - used to assess the configurations and slots alone without any morphing.

2.1. Matching the Cauchy number

The parameter representing the non-dimensional flexibility to match in this study is the Cauchy number (C_y), which is the ratio of the inertial force to the elastic force of the structure, see e.g. (Song et al., 2021):

$$C_y = \frac{\rho_w U^2 C_l W L^3}{2EI} \tag{1}$$

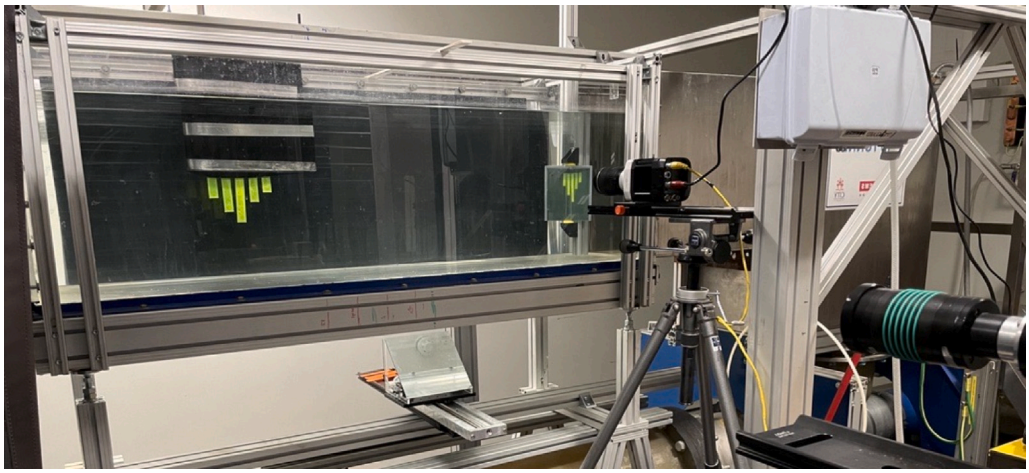

Fig. 2. Experimental setup.

In the case of the peregrine falcon the approximated Cauchy number based off the outer 25% of a primary feather (the region that exhibits the most bending) is $Ca = 0.593$. This value was calculated using (Eq. (1)) with EI - the Youngs Modulus (taken from Schmitz et al. (2015) and Williams (2019)), U - the typical cruise velocity ($11\,\mathrm{m\,s^{-1}}$–$15\,\mathrm{m\,s^{-1}}$, taken from Cornell Lab of Ornithology (2019)), C_l - the lift coefficient of the wingtip (taken from Tucker (1993)) and L, W the geometry of the wingtip (dimensions taken from Schmitz et al. (2015)). As the geometry of the flexible extensions were preset to be similar in scale to a peregrine falcon's primary outer 25% wingtip feather the Cauchy number was adjusted by selecting a material with the proper Young's Modulus, which is $0.196\,\mathrm{GPa}$ for the above described plastic. This then resulted in a Cauchy number of 0.582, suggesting the flexible extensions should behave similarly to the free endings of the falcon's primary feathers.

2.2. Wingtip configurations

Three deployment configurations were tested, along with a baseline case where the extensions were fully retracted within the wingtip (ref-type, see Fig. 3). The first configuration (I-type, see Fig. 3a) had each of the extensions deployed to their maximum length and resembled the configuration most common in wingtip extension research. This configuration is also comparable to nocturnal hunters such as the barn owl (see 1(a)). The second configuration (C-type, see Fig. 3b) mimics typical formations observed in soaring birds, where the feathers increase in length until the middle feather (largest extension). On a side note we observed that the length of the feathers are not symmetric about the central feather, thus none of the extension tips is directly in line with another. The third, configuration (Z-type, see Fig. 3c) derives from the same principal (not having any extension tip preceding another) but, instead has the extensions diminishing in length along the chord. The z-type configuration is additionally used to establish any special flow phenomena that occur from the natural configuration.

In the wingtip configurations shown we believe that the clamping conditions (a fixed cantilever beam) is comparable to the conditions of actual feathers, in that, due to the rounding of the wingtip the feathers are overlapped at the root and affix each other but allow for the individual bending of the feather tips at their free end.

3. PIV-methodology

In the first measurement series a $5\,\mathrm{W}$ CW Dantec Dynamics RayPower ($532\,\mathrm{nm}$ wavelength) fitted with laser sheet optics was positioned perpendicular to the mean flow upstream of an angled mirror affixed within the tunnel. Time Resolved Particle Image Velocimetry (TR-PIV) measurements of the secondary flow were conducted using a Phantom Miro M310 high speed camera (1280×800 pixel window size) equipped with a Tokina $100\,\mathrm{mm}$ macro lens focused on, via the mirror, the laser sheet. The images were taken at a sample rate of 100 fps and with the laser sheet set to a nominal thickness of $5\,\mathrm{mm}$ to ensure the particles remained in the sheet long enough to be cross correlated. The aperture was set to $f2.8$ and the exposure time of the camera was set to $3900\,\mu\mathrm{s}$. Plastic particles, of approximate diameter $20\,\mu\mathrm{m}$, were used as the seeding and placed into, and allowed to circulate around, the tunnel prior to testing.

As the extensions were only clamped at the root and free to bend and twist along the span a secondary highspeed camera with the same specifications given above was setup to observe the spanwise dynamics of the extensions. The camera was focused onto the tips of the extensions and was used to capture the zero flow and in flow extension curvature and tip locations. Where the effects of the slots alone without the self adaptive nature where tested the flexible extensions were replaced with the stiff extensions.

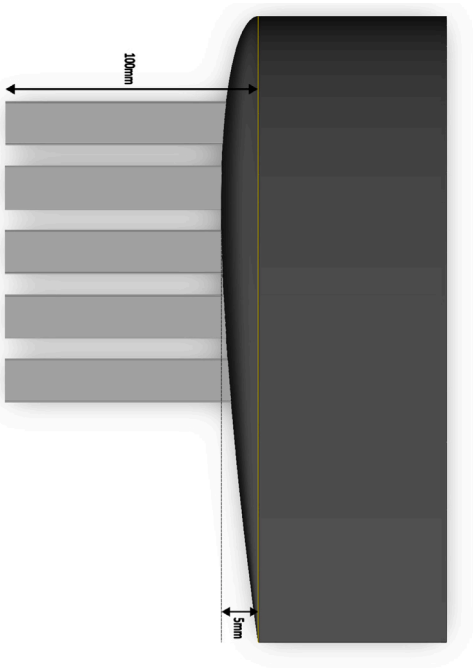

(a) Owl mimicking extensions (I-type)

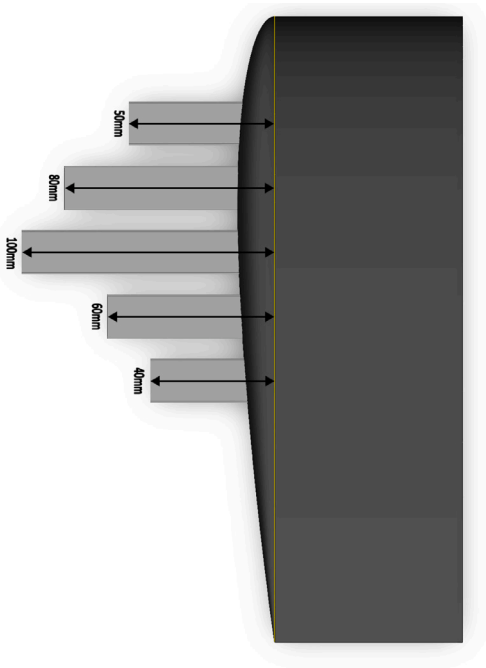

(b) Soaring bird mimicking extensions (C-type)

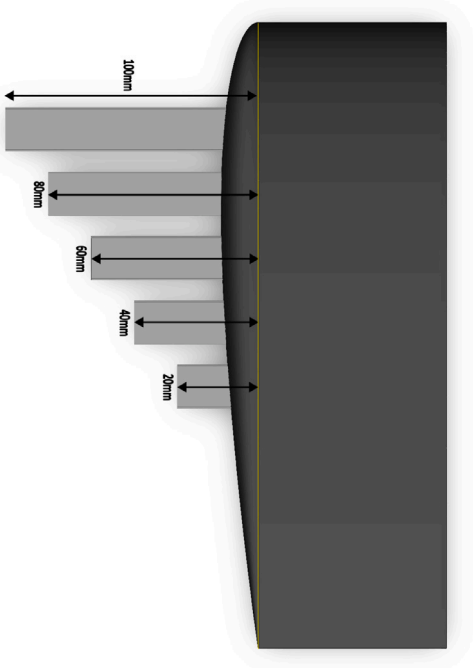

(c) Diminishing length extensions (Z-type)

(d) Fully retracted (planar) wingtip (ref)

Fig. 3. Wingtip configurations tested.

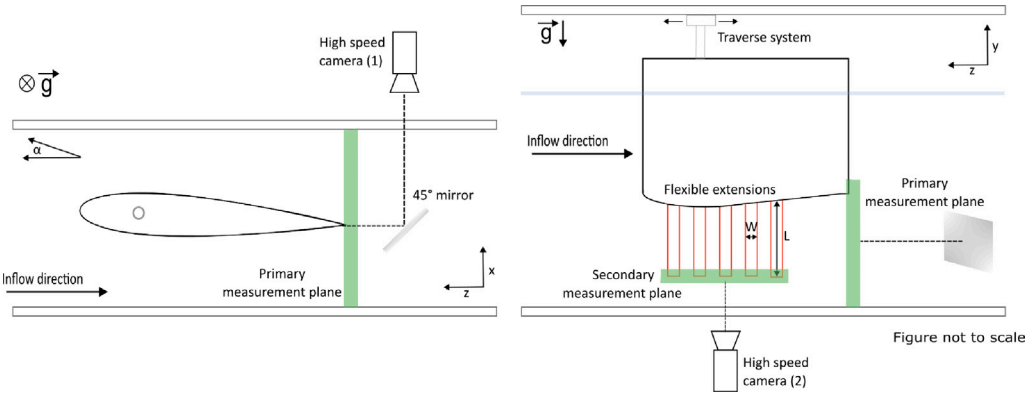

Fig. 4. Experimental setup (left: top-view, right: frontal view).

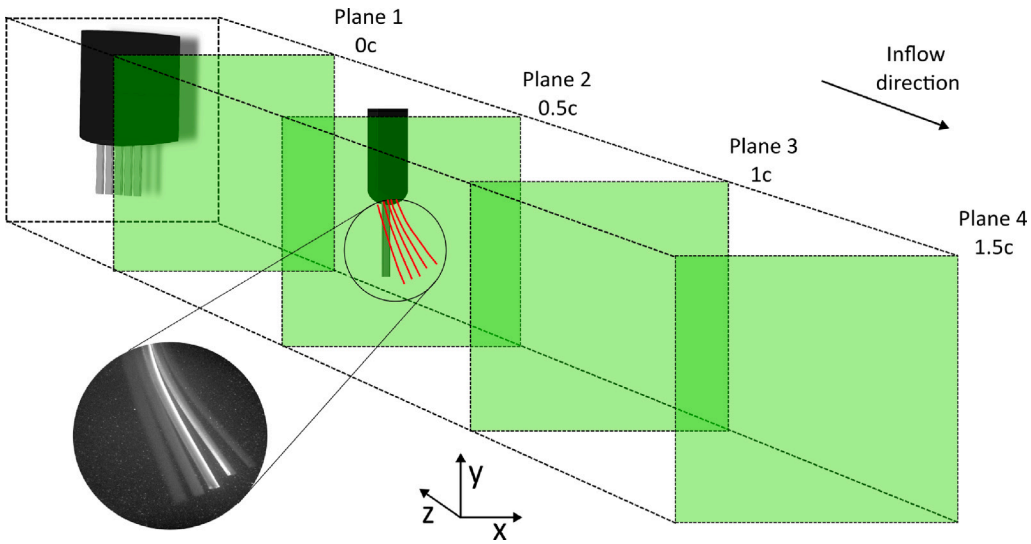

Fig. 5. Cross-sectional measurement plane at different positions downstream of the trailing edge.

Running over the top of the tunnel was a traverse system which the wing was mounted to. Between the experiments, the traverse was used to move the wing along the test section to the desired location upstream of the primary measurement plane. In each test the camera had the same field of view and remained focused on the middle of the laser-sheet which was stationary. The reference location for each test was taken when the trailing edge of the wing section is in the light sheet ($z = 0$ chord) (Fig. 4, Fig. 5)).

The captured images were processed using an in house *MATLAB* code which uses a classical 2D cross correlation method and post processing. Two passes of the images were conducted with a 50% overlap, where the interrogation window in the first pass was 32×32 pixels and in the second pass was 16×16 pixels (resulting in a final interrogation window size of $11.3\ \text{mm}^2$). Lambda-2 criterion was used to capture the vortices (Midmer and Bruecker, 2022) and more accurate detection of the vortex centres when compared with other tested methods for multiple core detection (Coletta et al., 2019). The results went through two filters to remove erroneous vectors and finally any missing vectors were interpolated from the local mean. Only the contours >-0.2 Lambda have been plotted in order to remove the background noise in the flow field.

Additional processing on *PIVlab* (Thielicke and Stamhuis, 2014) of the same images, using the same processing criteria as above, was used to assess the inter validity of both processing methods. The images processed with *PIVlab* were additionally used for the circulation calculations.

4. Results

Each of the wingtips with flexible extensions were tested at Reynolds numbers of $70k$ and $90k$, aside from the wingtips with the extensions retracted and stiff extensions were exclusively tested at a Reynolds number of $70k$. Herein the results shown are for a

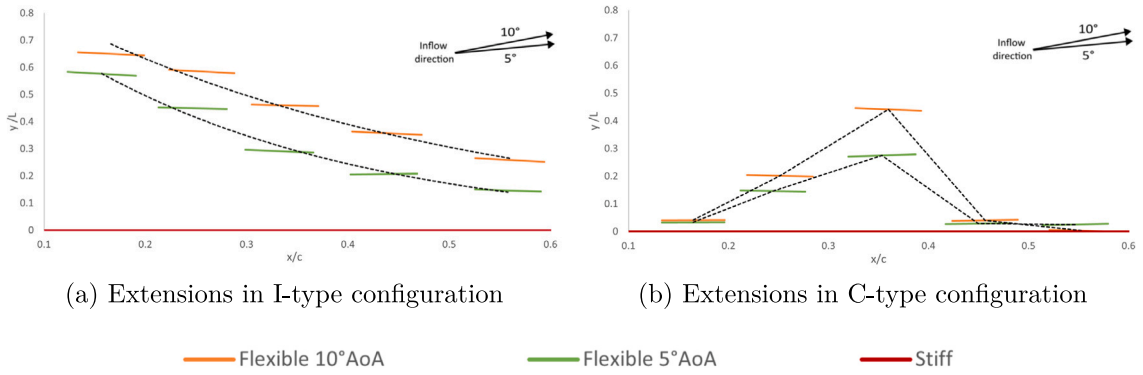

Fig. 6. Contours of the tips as seen from the lateral side relative to the pitched aerofoil, showing the upwards bending extensions and twist at Re = 70,000. (For interpretation of the references to colour in this figure legend, the reader is referred to the web version of this article.)

Reynolds number of $70k$ ($30\,\mathrm{cm\,s^{-1}}$) and an AoA of 10° unless otherwise stated. The $30\,\mathrm{cm\,s^{-1}}$ tests are shown as this matches both the Reynolds number and Cauchy number of the primary feather of a peregrine falcon, the other speeds and AOA tested however exhibited similar vortex spreading characteristics to the results shown.

4.1. Tip bending displacements

The deflection of the feather tips of the I-type and C-type configurations are shown to illustrate their bending in flow similar to what is observed for the wingtips of owls or thermal soaring birds. It also demonstrates the difference that changing the extension length alone can make. The tip locations of these two configurations also aid in the interpretation of the vortex interactions in Section 4.3.

After starting the flow, the flexible tip extensions bend upwards into their equilibrium position, where they remain in stable position. Fig. 6 shows the tip contours as seen from the lateral side, with the contours rotated with the plane of the observer fixed with the wing when changing the AoA. The contours are given for each respective configuration when the AoA is increased. The reference case with stiff extensions exhibit no bending regardless of AoA, therefore all tip contours are aligned with the x-axis. As was found previously (Midmer and Bruecker, 2022), the pattern formed by the flexible extensions remains consistent independent of AoA but the amount of curvature and tip displacement of the extensions increase clearly with AoA.

For the flexible extensions in the I-type configuration the cascading bending pattern can be approximated by an exponential decay (dashed lines Fig. 6(a)) from the leading to the trailing. The different amount of bending in this configuration could be used as a passive indicator of the lift distribution along the chord of the aerofoil, as shown by the correlation of the extensions' pressure distribution and the aerofoil's pressure distribution, see Liu et al. (2023). This is because all extensions have the same length and therefore their bending reflects the lift-forces acting on the cantilever beam type extension. Along the chord, the bending and twist of the extensions diminishes due to the downwash of the preceding extension decreasing the effective AoA and therefore reducing the bending and twist of the trailing one. In comparison, for the C-type configuration the leading three extensions show a linear increase in tip deflection with little separation between the two trailing extensions, which are barely bend. Herein, the increasing length of the free end of the extensions is reflected in the tip deflection pattern. Noticeably the magnitude of bending is not reaching maximum values as in the I-type configuration, despite having a more favourable vortex spread (shown later). The difference in tip deflection between the most and least bend extension in both configurations is approximately the same ($0.13c$) at 10° AoA but, significantly smaller for the C-type configuration ($0.08c$ compared to $0.13c$) at 5° AoA. The larger spatial separation of the tips (particularly between the first 4) of C-type configuration might result in a wider spacing between the individual tip vortices as shown later. Finally, the Z-type configuration showed similar bending of the extensions along the chord as shown for the I-type configuration. With regard to the flexible extensions it is not apparent that they undergo larger twisting with increased AoA (even with a higher local AoA), overall the contours do not show significant twisting in any configuration. Note that the reference vector of the free stream direction is shown to indicate that the extensions still have a positive angle of attack to the incoming flow direction.

4.2. Instantaneous flow field

An instantaneous snapshot of the flexible extensions in the C-type configuration is compared in Fig. 7 with measurements taken on the tip vortex of a live jackdaw 1 chord downstream. Despite the simplifications of the model used herein a clear relation to the real slotted wingtip can be observed; to the extent that similar relative inter-vortex core sizes and spacing for each test are observed. The different vortex core sizes in each case is due partially to the spacing of the feathers/extensions along the chord (meaning each vortex is at a different stage of development relative to the measurement plane) and also the lifting forces/downwash acting on each extension. A common centre of rotation of the 5 vortices emanating from each extension can also by identified from the

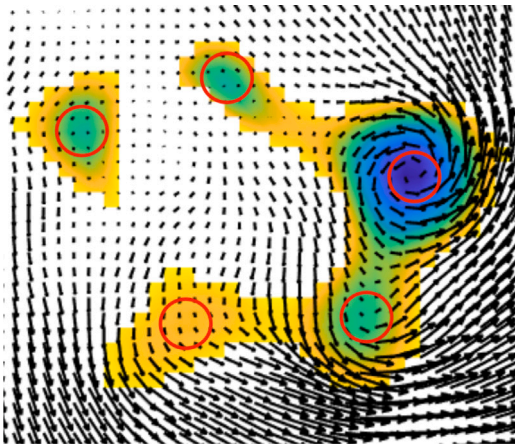

(a) Contours of lambda-2 criterion of the flexible extensions in C-type configuration at $Re = 90k$, 5° AoA at 1 chord downstream.

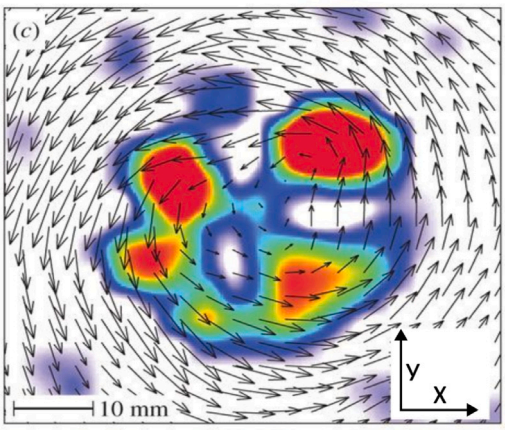

(b) Swirl strength from PIV of a jackdaw's slotted wingtip taken from (KleinHeerenbrink et al. 2017) with modified axis.

Fig. 7. Vortex pattern reconstructed in the wake of the bio-inspired wingtip in comparison to measurements of swirl strength in the wake of a life bird's wingtip. (For interpretation of the references to colour in this figure legend, the reader is referred to the web version of this article.)

diminishing vector magnitude concentric to the circumference created by the core centres (highlighted by the red circles). Fig. 7(a) is an exemplary snapshot taken across the whole measurement series and other test cases, but similar vortex spreading was also observed in the other test cases.

An instantaneous flow field is used to demonstrate the similarities to a real slotted wingtip due to the jittering of the vortices when viewed in a given downstream normal plane. This in turn causes the time averaged flow field to smear out some of the vortex cores.

Fig. 8 shows the vortex centre location movement of the four largest vortices in the C-type configuration at $Re = 90{,}000$, 5° at each downstream location. The vortex core locations were determined from local peaks in the lambda-2 criterion contour plots with sub-grid interpolation, see also the red circles indicating the core centres in Fig. 7(a). The spatial locations were then filtered to remove outliers beyond four standard deviations and then Gaussian smoothing was applied. Only the four largest cores are shown due to the ease of comparison between tests and the intermittent merging and large wandering of the smallest vortex core during the measurement period. The wandering observed, despite the additional interactions with the other cores follow a similar linear increase across the downstream locations tested herein to the findings of other studies (Cheng et al., 2019; Heyes et al., 2004). However, attributed to the instabilities caused by multiple vortices in close proximity, each core has a larger wandering amplitude than in the other studies where only a singular tip vortex was studied (Heyes et al., 2004; Cheng et al., 2019). Fig. 10b shows the normalised wandering amplitude of the five cores with respect to downstream location as discussed, the fifth (weakest) core exhibits the largest amount of wandering relative to the other cores. But, cores one through four all have similar wandering amplitudes across each measurement plane (between 0.005–0.035). In all cases the amplitude of wandering increases with downstream location (also observable in the increasing radii of each core centre location, Fig. 8) due to each vortices self instability (Cheng et al., 2019) and the shear between the vortex cores. Across the AoA and Reynolds numbers tested the same trends that have previously been observed- the wandering amplitude decreases linearly with increasing AoA and increases linearly with increasing Reynolds number (Cheng et al., 2019)- are also present (not shown). In each case the motion of wandering is dominated by the component perpendicular to the circumference of rotation (perpendicular to the wandering trajectory Fig. 10, also see Fig. 13).

Fig. 9 shows the instantaneous vortex centre location in x,y coordinates of core 2 relative to its movement throughout the measurement series. To assist interpretation of the location of the vortices over time, 2-D probability density function plots (PDFs) of the location of each core in the x-y-domain, at each downstream location for the C-type configuration at $Re = 90{,}000$, 5° test case can be found in Appendix A (Figs. 15–18). The PDFs were produced by first, dividing the scatter plot into a 10×10 grid and finding the frequency the core centre was in a given grid space. This was further interpolated to a finer grid (100×100) and smoothed, resulting in zoomed-in views of iso-contours of the core centre location PDF.

The non-dimensional frequencies from the I-type and C-type (taken from the first core) configurations are presented in 1, overall the I-type configuration exhibits lower oscillations and therefore has a more stable vortex than the largest vortex from the C-type. Note only the most dominant core frequency from the C-type configuration is presented, the other weaker cores showed greater oscillatory motion. The larger oscillation of the cores indicates instabilities that would promote a more rapid wake destruction, but at the cost of greater aeroacoustics. In contrast the I-type configuration, with its single and more stable core, will be relatively quieter but may have a longer persisting wake.

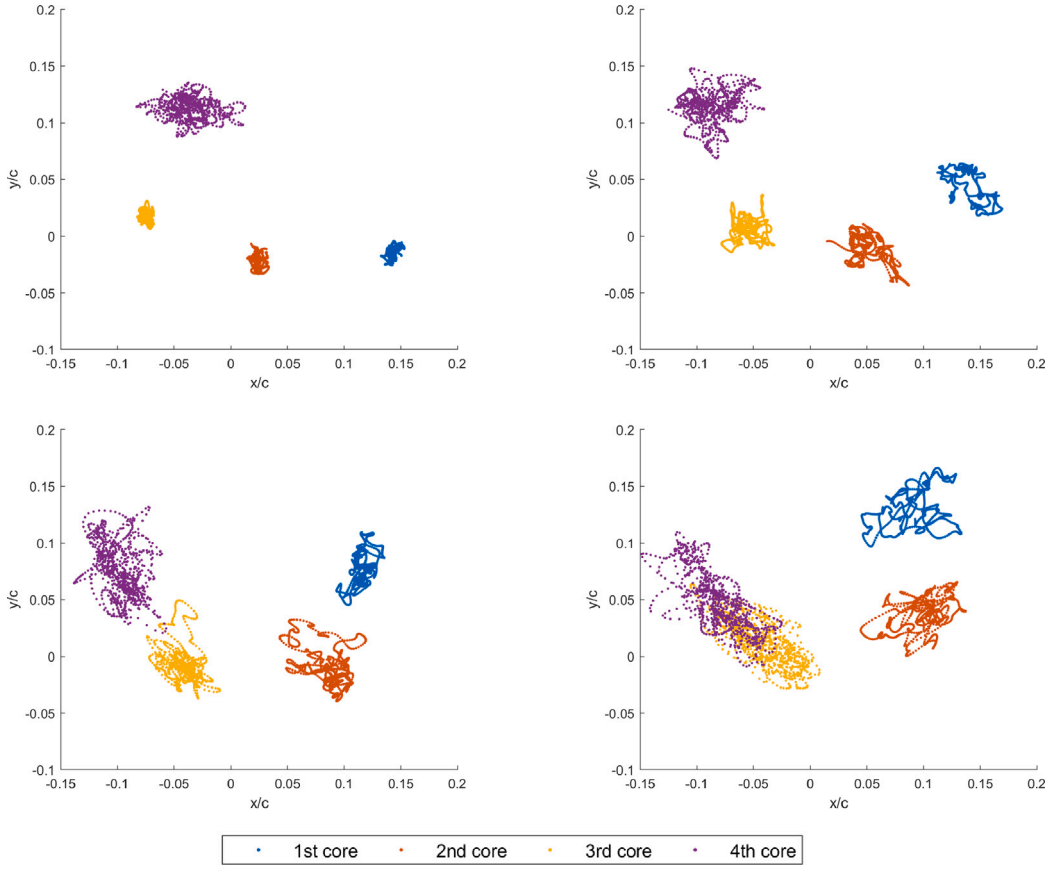

Fig. 8. Scatter plots of the instantaneous vortex core locations of the four strongest vortices in C-type configuration at $Re = 90{,}000$, 5° AoA and $0, 0.5, 1$ and 1.5 chords downstream respectively. (For interpretation of the references to colour in this figure legend, the reader is referred to the web version of this article.)

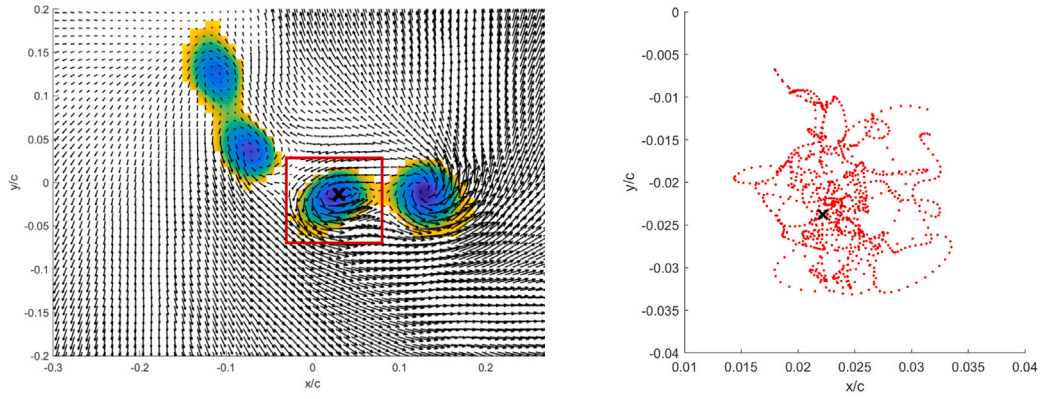

(a) Instantaneous flow field and contours of lambda-2 criterion, focusing on core 2 (red box).

(b) Zoom-in view of the detected core locations of vortex core #2 over time.

Fig. 9. Comparison of the instantaneous vortex centre of core 2 relative to the movement over time (C-type configuration at 0 chords downstream, $Re = 90{,}000$, 5°). In both cases the 'X' is the core centre. (For interpretation of the references to colour in this figure legend, the reader is referred to the web version of this article.)

The relative position of the four strongest vortex cores in the cross-section changes when moving further downstream as shown in Fig. 10. The projection of the trajectory of each core shows a segment of a common centre of rotation. This results in a spiralling structure of the multiple vortices (see KleinHeerenbrink et al. (2017)) which draw closer together and eventually amalgamate into

Table 1
Non-dimensional vortex oscillating frequency of I-type and C-type configurations downstream.

Configuration	Strouhal number			
	0.0c	0.5c	1.0c	1.5c
I-type	0.225	0.225	0.225	0.375
C-type (1st core)	0.160	0.315	0.315	0.375

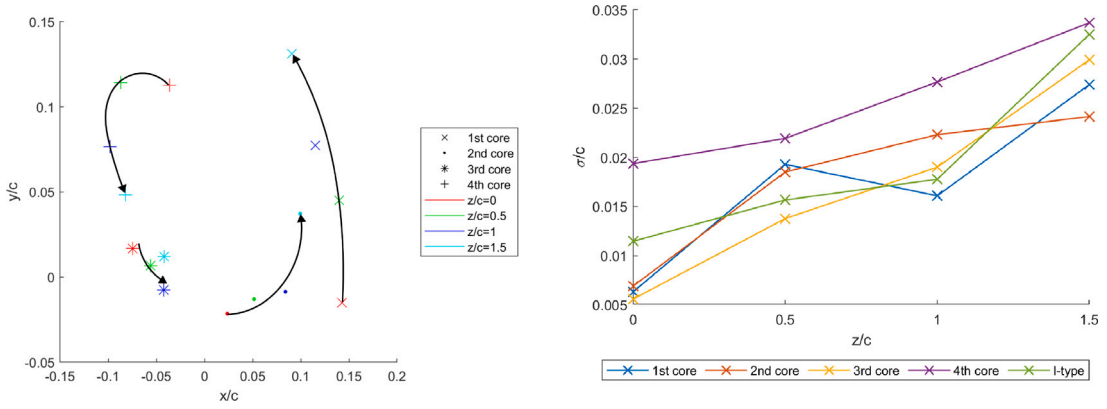

Fig. 10. Left: projection of the trajectories of the multiple vortex cores in the radial plane, indicating the spiralling structure of the cores around a common centre; right: increase of the amplitude of core jittering (wandering) motion with downstream distance. Both plots are for the C-type configuration at $Re = 90{,}000$, 5° AoA and $0, 0.5, 1$ and 1.5 chords downstream. (For interpretation of the references to colour in this figure legend, the reader is referred to the web version of this article.)

a single vortex further into the wake. The reducing distances between cores further exacerbates the instabilities (which are already greater than for counter rotating vortices, Leweke et al. (2016)) and again describes the increasing wandering amplitude further downstream.

The critical non-dimensional separation for vortex merger open to interpretation however, typical values for cores of equal strength are from $d/r \approx 3-4$ (numerically and experimentally by Christiansen (1973) and Meunier et al. (2002)), where d is the separation and r the core radius. In the C-type configuration tests with the circular vortex arrangement the non-dimensional separation falls within this range, which is why the cores amalgamate downstream. It has also been shown (although for 2 pairs of counter rotating vortices) that co-rotating vortices undergo a wrapping process at an optimal separation distance, in which rapid dissipation occurs (Cho et al., 2020). Due to this, and due to the multiple unequal sized vortices that merge quicker than if they were equally sized (Berténi and Graham, 2007), it is also stipulated that the wake diminishes quicker than in this circular vortex pattern.

4.3. Time averaged flow field

Fig. 11 is each of the configurations vortex interactions at the trailing edge. In all of the cases where the extensions are present in the flow the vortices can be seen to be dislocated outboard, away from the wing (-y direction) and vertically upwards (-x direction) away from the wing surface.

Overall, the wingtip in the I-type configuration dislocates the vortex away from the wing and reduces the core strength/size relative to when no extensions are deployed 11(d). The slotted tip also allows part of the roll-up from the pressure side to pass through the slots, which is beneficial in generating additional lift by energising the flow in the suction side tip region (Tangermann et al., 2022). This also provides an explanation to why the core strength is slightly decreased relative to the reference wing.

It is interesting to see that, while the I-type configuration does show a distinct separation of the feather tips, the vortices do not split but form a continuous vortex sheet that rolls-up into a single core at the outermost region, see also our previous study (Midmer and Bruecker, 2022). It is suggested that the exponential decay of the bending and the individual downwash generated after each extension leads to nearby passages of the tip vortices, which then merge and form a singular vortex (Fig. 11(a)). A possible benefit of such smooth formation could be relevant for the aeroacoustic impact of tip vortex formation. It is speculated herein, that the continuous roll-up into the single vortex, dislocated outboard and upwards away from the wing, could produce less acoustic noise than formation of multiple small vortices that interact with each other. Following this speculation, this could provide more beneficial for owls, where reducing acoustic noise is paramount.

The other two extension configurations (Figs. 11(b) and 11(c)) do make full use of the self adaptive and spatial separation of the extensions and 4–5 individual vortex cores can be identified emanating from each of the flexible extension tips. For the C-type configuration (Fig. 11(b)) the cores get progressively stronger, where the leading tip vortex is the weakest, until the final vortex

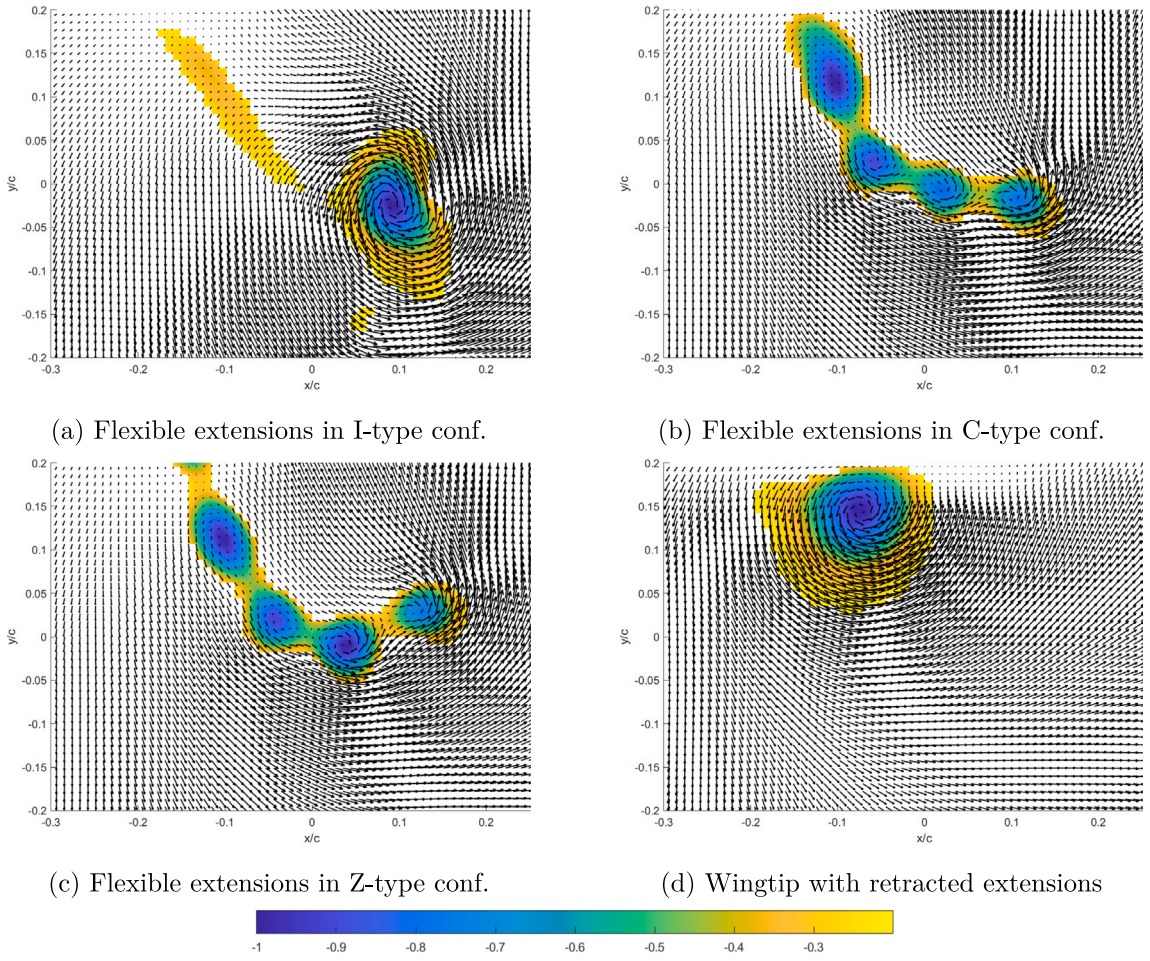

Fig. 11. Contours of lambda-2 criterion, 0 chords downstream at $Re = 70{,}000$ and 10° AoA. (For interpretation of the references to colour in this figure legend, the reader is referred to the web version of this article.)

which is both larger in size and strength (as discussed in Section 4.2). This is not the case for the Z-type configuration where each vortex is of relatively the same size and magnitude. The absence of one expected vortex core in Fig. 11(b) is attributed to the definition of minimum core radius in the lambda-2 criterion calculation, along with the averaging of the flow field, which has not been able to distinguish the two vortices off the trailing extensions apart and has therefore resulted in the larger, elongated vortex sheet seen. A common centre of rotation, for the configurations with spatially separated tips, can also be observed to be developing.

Fig. 12 shows the downstream measurement planes of I-type and C-type configuration for comparison of the two natural wingtip types. The vortex produced by the I-type configuration remains relatively stable (with only the expected migration of the core inboard) and a continuous size and strength across the downstream locations. For the C-type configuration the average flow field suggests the originally separate, individual, vortices begin to coalesce together until at 1.5c downstream, where the merging of the final two cores can be seen (Fig. 12(f)). In each case the vortices converge in pairs, dictated by the weaker of the two cores migrating towards, and merging with the stronger core. At 1.5c downstream the final vortex of the C-type configuration remains smaller than that from the I-type configuration. This suggests the C-type configuration is better optimised for wake destruction and this could be further tuned by altering the spatial locations of the tips for different Reynolds numbers and AoA.

The C-type configuration also exhibits along the wake a larger inboard motion than the stable vortex in the I-type configuration. The reduced length of the extensions of the C-type configuration cause the individual tip vortices to be initially produced closer to the wing (compare Figs. 11(a) and 11(b)). In addition, the vortices experience the inboard motion ($+y$) caused by self-induction and rotation around the common centre which also brings the final core more inboard.

Similar findings were found for the other AoA and velocities tested, where individual vortices were produced from each extension tip and the velocity and AoA influenced the downstream spatial location where they merged. The formation and merging of the vortices can also be seen in other studies where the slotted multi-winglet was similarly shown to reduce total vorticity in the near

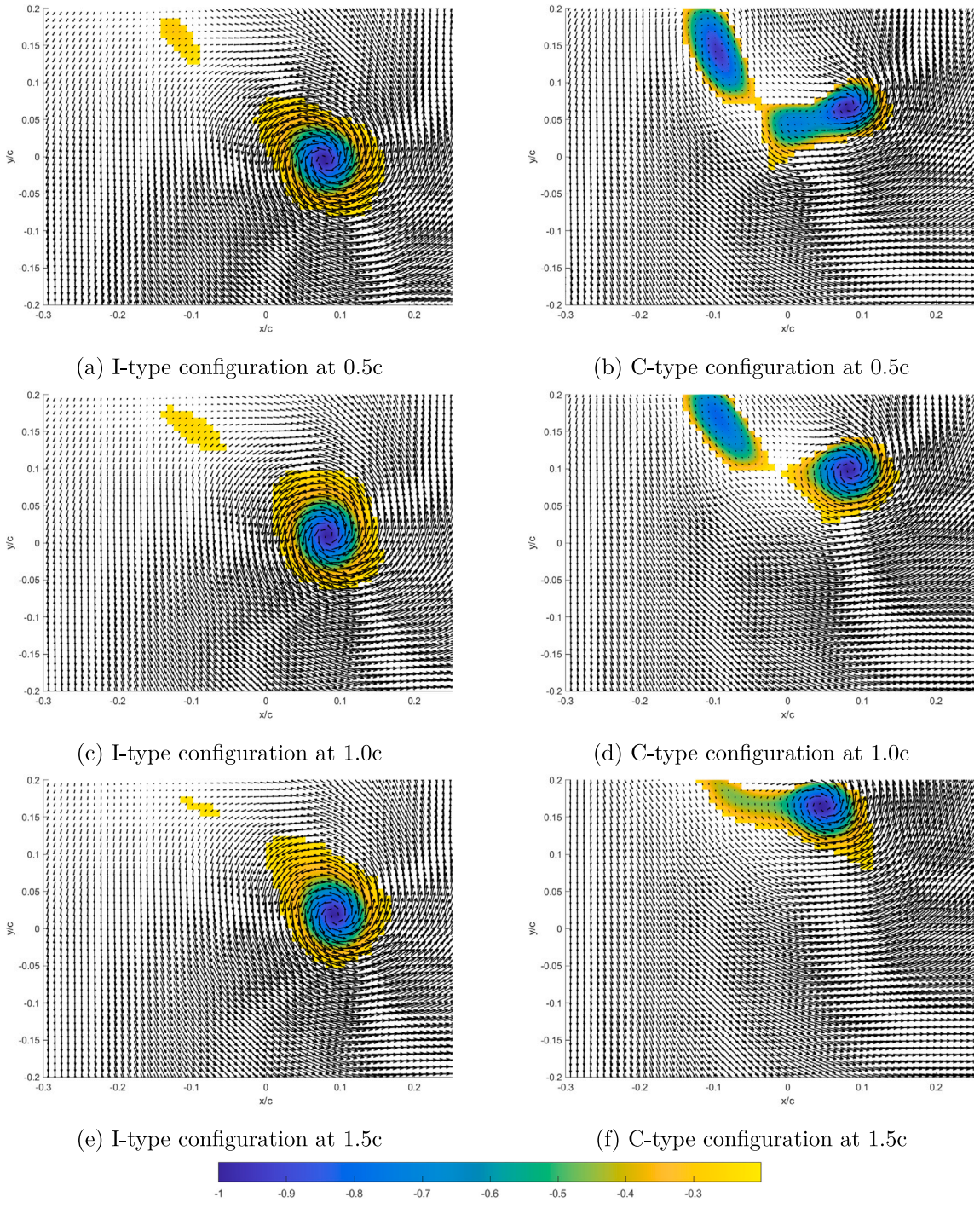

(a) I-type configuration at 0.5c

(b) C-type configuration at 0.5c

(c) I-type configuration at 1.0c

(d) C-type configuration at 1.0c

(e) I-type configuration at 1.5c

(f) C-type configuration at 1.5c

Fig. 12. Contours of lambda-2 criterion, in the fully deployed and bird-like configurations at $Re = 70{,}000$ and 10° AoA. (For interpretation of the references to colour in this figure legend, the reader is referred to the web version of this article.)

wake region (Hui et al., 2021). Based off the core sizes of each of the configurations at 1.5 chords downstream the use of a slotted wingtip does promote the reduction of wake vorticity. This could be beneficial in aviation when the reduced vortex strength would allow to increase take-off and landing frequency on airports.

All the above shown results represent the time-averaged flow fields. However the instantaneous PIV flow maps show strong fluctuations of the location of the vortices and their merging process. Therefore, the data set was analysed using the method of

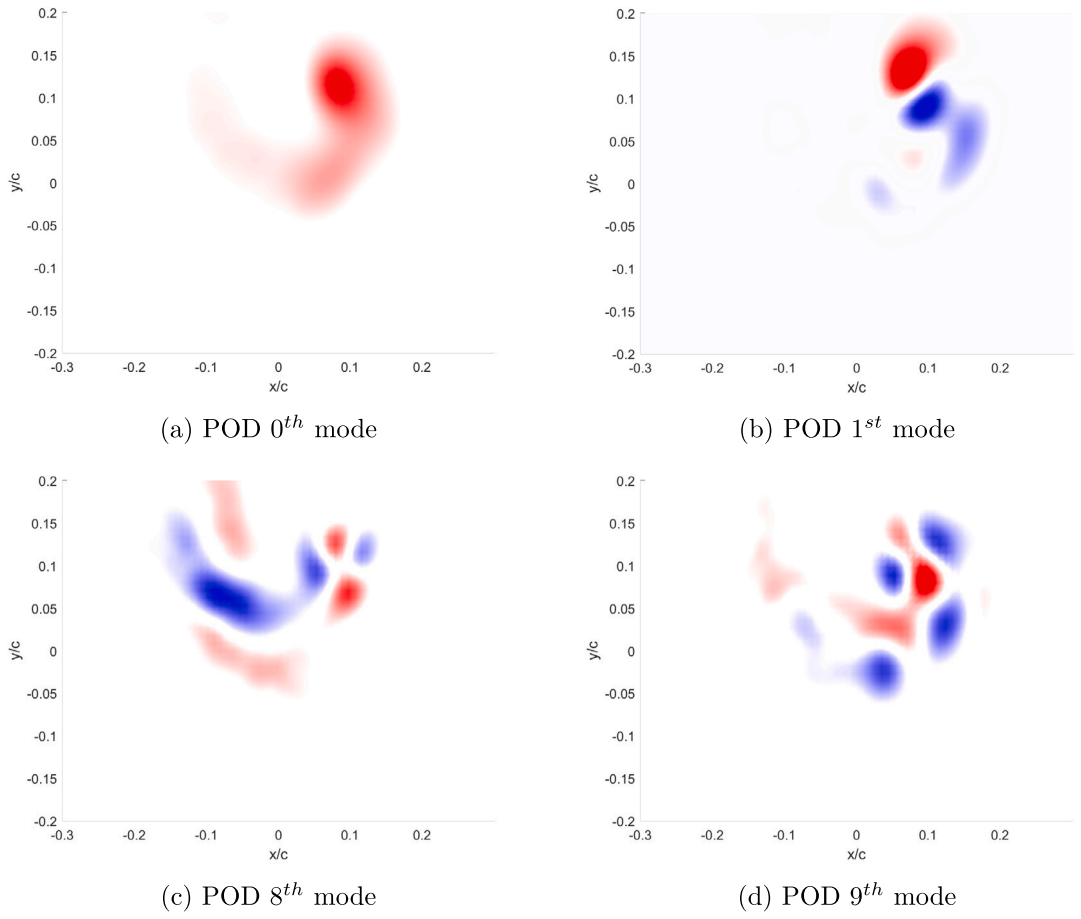

Fig. 13. Proper orthogonal decomposition modes at $z/c = 1.0$ in the $Re_c = 70{,}000$ and 10° AoA test. (For interpretation of the references to colour in this figure legend, the reader is referred to the web version of this article.)

Table 2
Energy and frequencies of the POD modes at $1.0c$ downstream.

	Mode									
	0th	1st	2nd	3rd	4th	5th	6th	7th	8th	9th
Energy (%)	72.25	5.99	2.88	1.78	0.91	0.87	0.83	0.73	0.68	0.59
Strouhal number	4.90	2.00	0.11	1.71	3.06	1.37	2.09	0.77	5.11	0.41

Proper Orthogonal Decomposition (POD) to find out the most dominant modes and their temporal variance of energy. Fig. 13 shows the results of Proper Orthogonal Decomposition (POD) analysis of the lambda-2 fields. The 0th, the 1st, 8th and 9th, modes are given, with the rest of the modes in Appendix B (Fig. 19). The 0th (average) mode identifies the four strongest cores clearly and the rotational path can be defined. As in the instantaneous flow field (Fig. 7) a dominant vortex is identifiable, both in size and magnitude, and the other vortices diminish in strength in a clockwise direction from 1st vortex. Comparable results were found in the other downstream locations tested (not shown) and the development of the common rotational centre of the cores were as also indicated in Fig. 10a. The other test configurations, Reynolds numbers and different AoA also had similar 0th modes with multiple vortex strength and a dominant vortex. While the 0th mode shows the mean field, the 1st mode is indicative for the oscillation of the vortex locations in the individual instants of the recorded sequence. Fig. 13b is the 1st mode at 1.0 chord downstream however, similar characteristics are found in the other downstream locations and modes, where the higher modes predominantly identify the motion of the two strongest cores and the lower modes of the remaining cores and circulatory motion and wandering of the cores. The two major energy lobes indicate the dominant oscillatory motion of the first vortex in the tangential direction of the virtual

Table 3
Downstream near wake circulation at different AoA, normalised with the deployed extension area.

Configuration	0.0c, AoA 5°	0.5c, AoA 5°	0.0c, AoA 10°	0.5c, AoA 10°
I-type	1.24E−03	9.13E−04	2.21E−03	1.44E−03
C-type	2.06E−04	2.17E−04	9.02E−04	2.77e−04

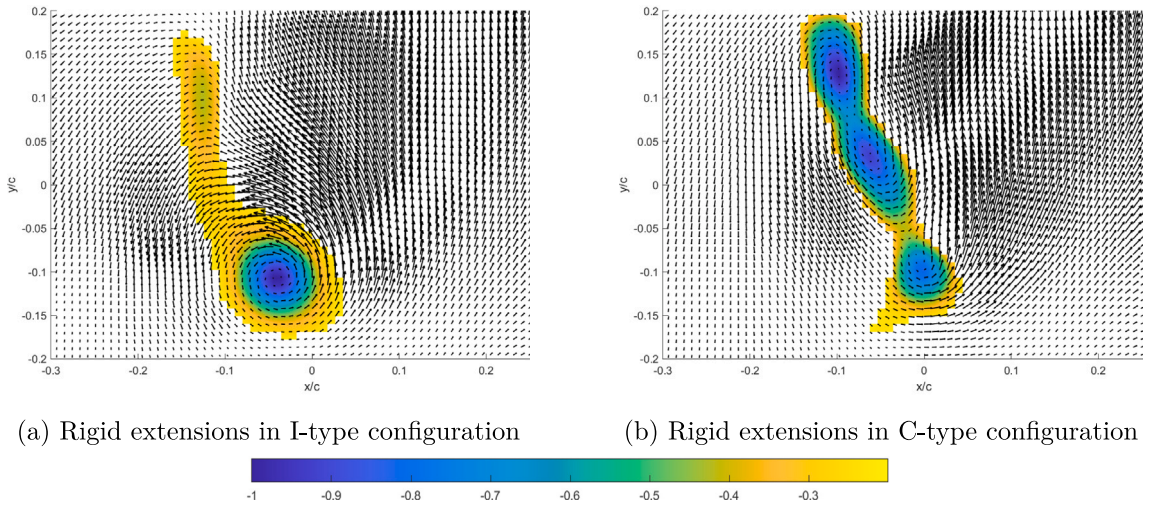

Fig. 14. Contours of lambda-2 criterion, 0 chords downstream at $Re = 70{,}000$ and 10° AoA of the rigid extensions. (For interpretation of the references to colour in this figure legend, the reader is referred to the web version of this article.)

circle, along where the cores are aligned (also discussed in Section 4.2). Similar structures were observed in the higher modes for the other vortices where there was an oscillatory motion tangential to the circulation of the cores as a whole. The energies and associated frequencies of each of the modes are given in Table 2. Table 3 shows the downstream near wake circulation (0.0c and 0.5c) of the I and C type configurations, note that 0 chords downstream indicates the trailing edge of the aerofoil and the extensions do not cover the full chord length. In each respect both configurations are normalised with the extension area exposed to the flow. In both angles of attack and downstream locations the C-type configuration greatly reduces the circulation compared to the I-type, further demonstrating how each wingtip type is optimised for different purposes.

4.4. Comparison to rigid extensions

For comparison, experiments were also done with rigid, planar extensions (which exhibited no bending) in the same configurations. Fig. 14(a) demonstrates the same flow characteristics for the rigid extensions as for the flexible extensions of the same configuration (Fig. 11(a)) but, due to their rigidity the produced vortex is only dislocated horizontally away from the wing and not vertically. In this instance no benefit from the slotted wingtip can be observed and it can be compared to a conventional wing section with an increased span but, without the benefit of increased lift.

The use of a C-type configuration alone, despite not having any non-planar aspect, can still be seen to break up the tip vortex in to smaller cores (Fig. 14(b)), although not as effectively as the flexible extensions in the same configuration (Fig. 11(b)). Again, as the extensions protrude parallel to the wing span the vortices are only dislocated horizontally away from the wing and therefore a circular pattern with a common rotational centre is not formed. The flexible extensions in the C-type configuration are able to separate out the vortices most effectively as there is a separation of the tips in all the (x y and z) planes. This is in contrast to the rigid extensions in the C-type configuration that have no separation in the y plane and the I-type configuration that has no tip separation in the y or z planes.

To further maximise the spreading of the individual vortices the emanating point of the extensions can be positioned at differing heights on the thickness of the aerofoil. This is also similarly achieved in nature by the camber of a birds wing, resulting in the root of the wingtip feathers being offset vertically along the chord.

5. Conclusion

Flexible extensions mimicking feather tips protruding out of a wingtip have been tested for their influence on the formation of the tip vortex flow in the wake of an aerofoil. Three different deployment configurations have been studied, which resemble

configurations observed in nature. For zero AoA there is no bending of the extensions and flow is similar as if using rigid extensions. When increasing the AoA, the flexible extensions start to bend vertical upwards with increasing AoA in a proportional manner, reaching typical tip displacements of up to approximately 50 percent of their free length at AoA of $10°$. These results were found for similar geometrical and dynamic conditions of the extensions when compared to the natural ones of birds, keeping the Cauchy-number, Reynolds-number and scales similar as in nature. As a result of their morphing into curved shapes, the tips spread in both spanwise and vertical directions in different magnitudes, leading to the formation of a group of separated tip vortices, spreading the roll-up of vorticity into several cores, as proven by the PIV-measurements in cross-sectional planes downstream. When the extensions have the same length (I-type), the tip deflection decays from leading to trailing feather in a continuous manner, which is explained by the downwash effect. The preceding feather induces on the flow its own wake which approaches the next extension and results in a lower (extension) AoA. As observed, the spreading is small and the cores merge early in a vortex sheet with a smooth roll-up into a singular vortex, which is dislocated further outboard and upwards away from the wing.

Varying the length of the flexible extension along the chord in the C-type configuration (similarly seen on thermal soaring birds) was found to improve the vortex spreading in the lateral and vertical directions, with the cores forming nearly in a circular pattern in the wake- as also measured in live bird experiments. The vortices were observed to form spiral trajectories in the wake around a common centre, which persisted further into the wake for larger Reynolds numbers.

The quasi-circular arrangement in the cross-sectional plane in the C-type configuration is speculated to be most effective in reducing induced drag and to lead to a more rapid vorticity disintegration within the wake. However, the mutual interaction of the spiral-type vortices and their instabilities leads to oscillatory wandering of the cores and might contribute to the production of aeroacoustic noise of the wingtip. On the other hand, the smooth merging into a vortex sheet with a final roll-up into a singular vortex (as observed for the I-type configuration) leads to a more stable core with lower vorticity and is expected to have less acoustic noise. This argument is to be proven in further experiments, which is part of our future work. As a conclusion of such a hypothesis, the flexible extension may help to improve the aerodynamic performance for high AoA situations while also reducing the tip noise, based on the above conclusion.

It is evident that a self adaptive wingtip can reduce the induced drag but also, depending on the desired requirements, the wingtip might be tailored to minimising noise or to promote rapid dissipation of the vorticity in the wake. We speculate that these differences in optimisation transfer to different types of slotted wingtips in nature namely, the I-type configuration to nocturnal hunters (such as the Barn Owl) where stealth is more beneficial and the C-type configuration to thermal soaring birds (such as the Turkey Vulture) where tight manoeuvrability and wake control is more important. These aspects can be applied to commercial aircraft where quicker dissipation of tip vortex vorticity in the wake would reduce the time interval between aircraft taking off/landing, or for UAVs in urban environments where minimising noise pollution is of major concern.

Note that there are additional aspects such as wing camber which determine the position of the tips of birds feathers under aerodynamic load and therefore may contribute further to the dislocation of the vortices, which is not considered herein. Furthermore, birds are able to control the feather overlapping (similar to how bird feathers stay together, Wissa et al. (2015)), therefore they can also control how far the free ends of the feathers stand out into the flow (i.e. the extension length). This might help to adapt the wingtip vortex formation in the way described herein. Similar adaptations could be possible in aircraft with the pneumatic control of the feather deployment mechanism presented herein. Finally, materials with adaptive stiffness could be used to bridge the gap between a rigid spanwise wing extension and a flexible self-adaptive wingtip, with the possible benefits described. The former would benefit the cruising situation while the latter the take-off and landing situation.

CRediT authorship contribution statement

Alden Midmer: Writing – review & editing, Writing – original draft, Methodology, Investigation, Formal analysis, Data curation, Conceptualization. **Christoph Brücker:** Writing – review & editing, Writing – original draft, Validation, Supervision, Resources, Project administration, Methodology, Investigation, Funding acquisition, Formal analysis, Data curation, Conceptualization.

Declaration of competing interest

The authors declare that they have no known competing financial interests or personal relationships that could have appeared to influence the work reported in this paper.

Data availability

Data will be made available on request.

Acknowledgements

The authors would like to acknowledge Keith Pamment for his assistance in manufacturing the mounting system for the wing. The position of Professor Christoph Bruecker is co-funded as the BAE SYSTEMS Sir Richard Olver Chair and the Royal Academy of Engineering Chair (grant RCSRF1617/4/11) which is gratefully acknowledged. Alden Midmer is co-funded by City, University of London and BAE SYSTEMS which is gratefully acknowledged.

Appendix A

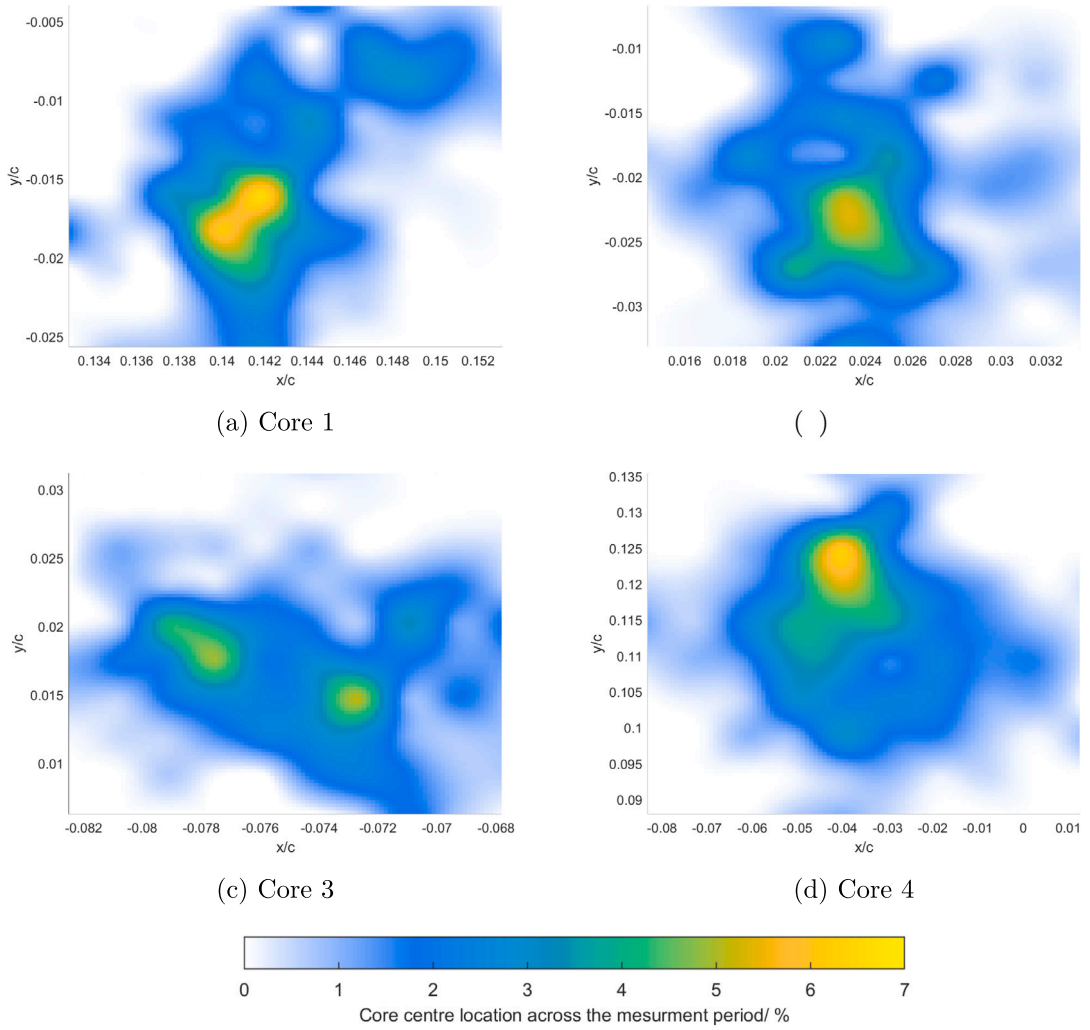

Fig. 15. Zoomed-in view, 2D probability density function of the x,y locations of the 4 strongest cores at Re_c = 90,000 in the cross-sectional plane at a z-position of 0 chords downstream of the trailing edge. Note the physical area of each plot is not equivalent and is instead scaled to fit the range of core centre movement. (For interpretation of the references to colour in this figure legend, the reader is referred to the web version of this article.)

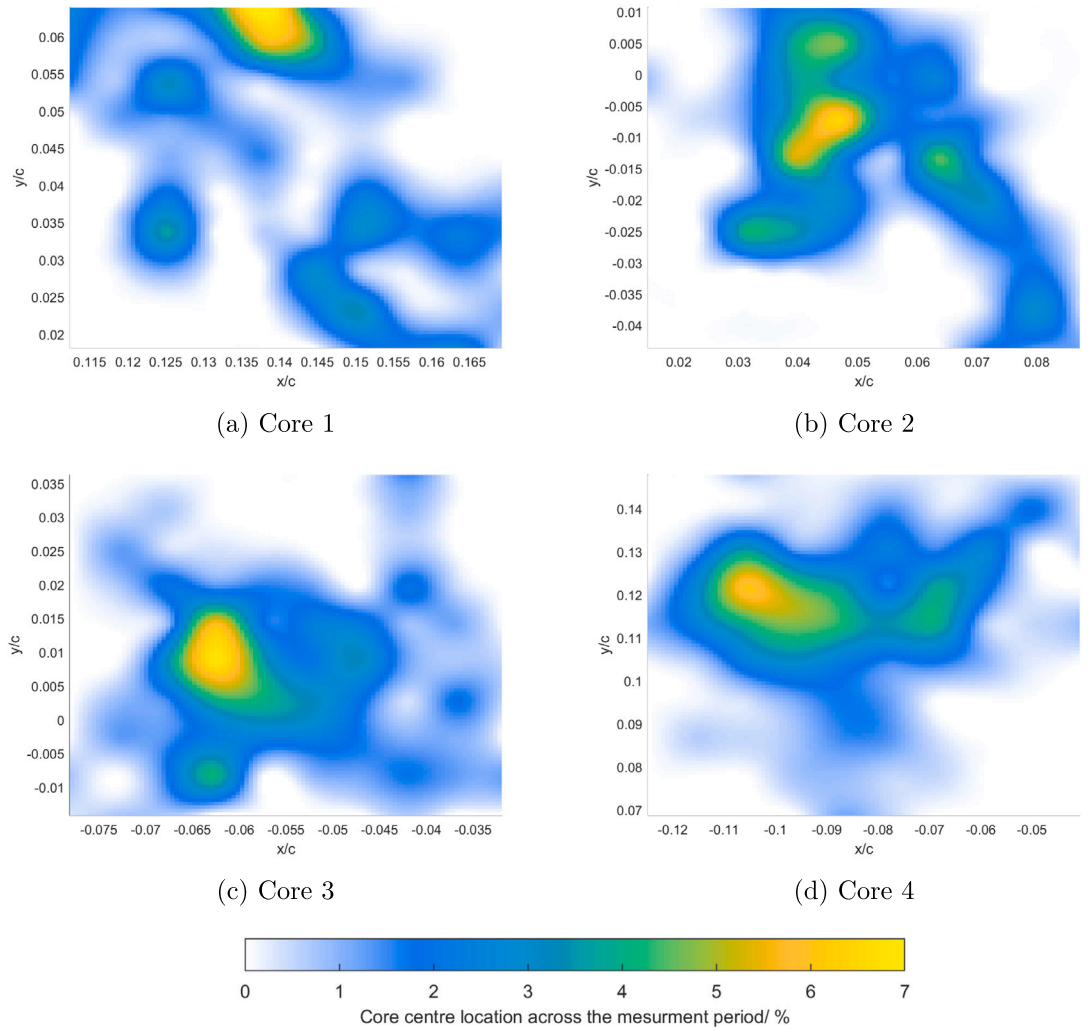

Fig. 16. Same as in Fig. 15 but now at 0.5 chords downstream. (For interpretation of the references to colour in this figure legend, the reader is referred to the web version of this article.)

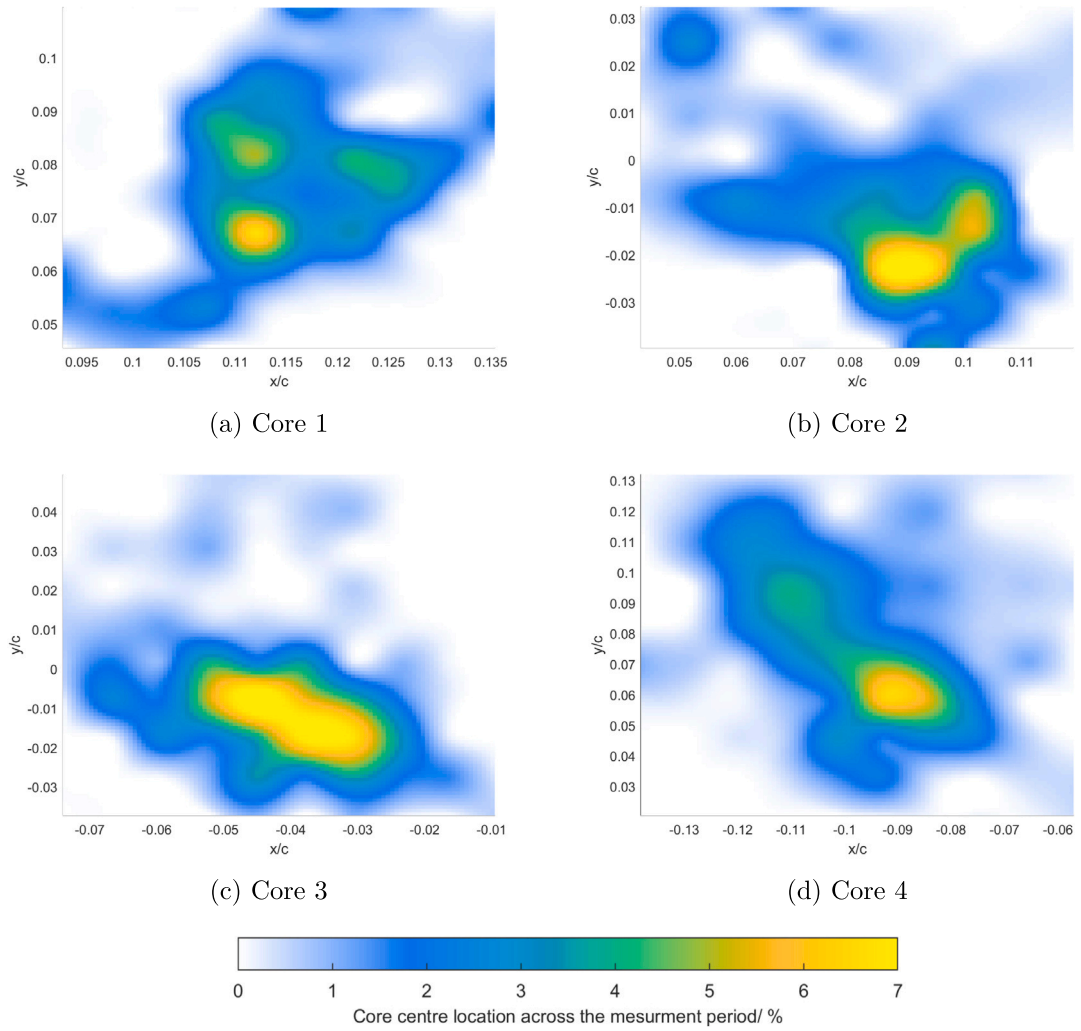

(a) Core 1 (b) Core 2

(c) Core 3 (d) Core 4

Fig. 17. Same as in Fig. 15 but now 1 chords downstream. (For interpretation of the references to colour in this figure legend, the reader is referred to the web version of this article.)

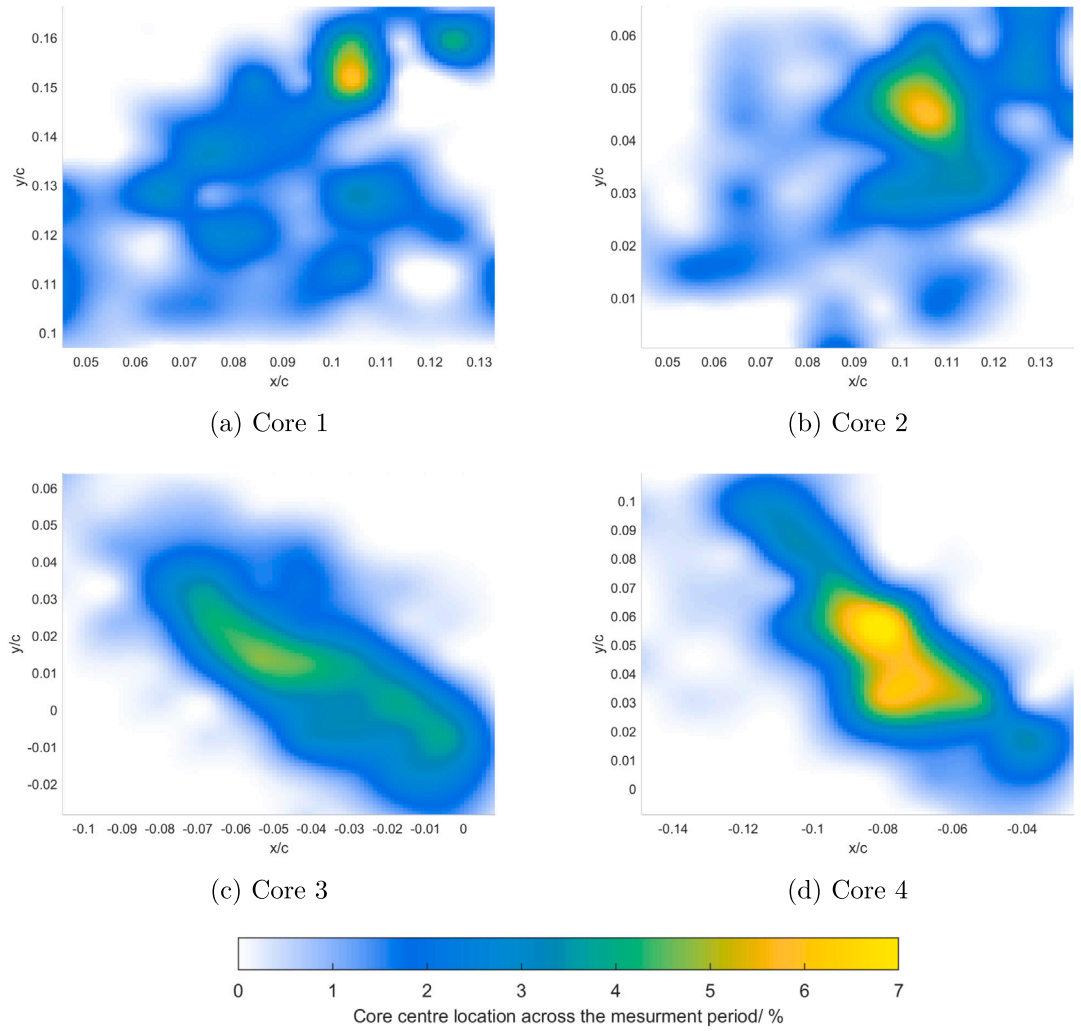

Fig. 18. Same as in Fig. 15 but now 1.5 chords downstream. (For interpretation of the references to colour in this figure legend, the reader is referred to the web version of this article.)

Appendix B

See Fig. 19.

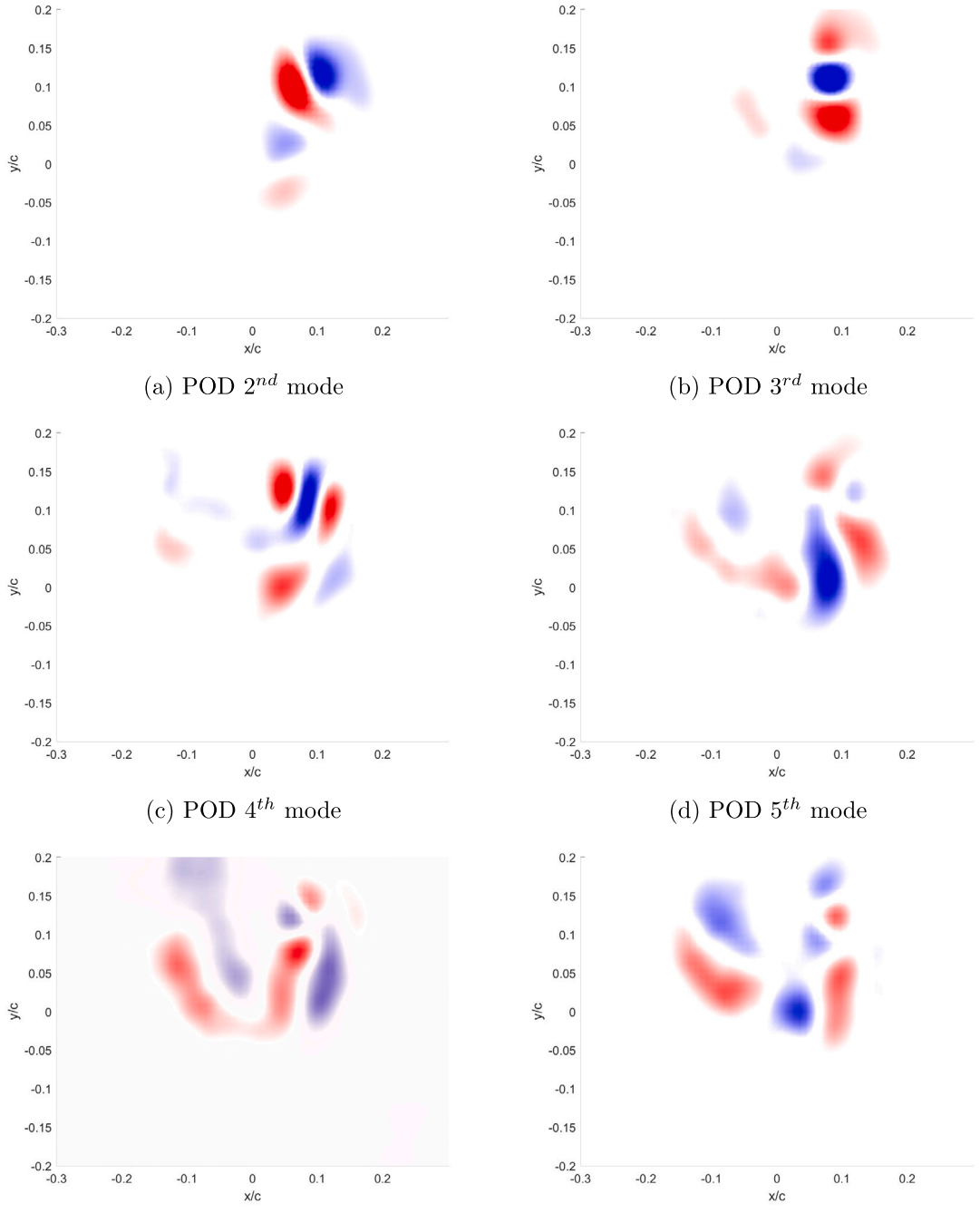

(a) POD 2^{nd} mode

(b) POD 3^{rd} mode

(c) POD 4^{th} mode

(d) POD 5^{th} mode

(e) POD 6^{th} mode

(f) POD 7^{th} mode

Fig. 19. Proper orthogonal decomposition modes at $z/c = 1.0$ in the $Re_c = 70{,}000$ and 10° AoA test. (For interpretation of the references to colour in this figure legend, the reader is referred to the web version of this article.)

References

Berténi, T., Graham, W., 2007. Experimental observations of the merger of co-rotating wake vortices. J. Fluid Mech. 586, 397–422.

Cheng, Z., Qiu, S., Xiang, Y., Liu, H., 2019. Quantitative features of wingtip vortex wandering based on the linear stability analysis. AIAA J. 57 (7), 2694–2709.

Cho, J., Lee, B., Misaka, T., Yee, K., 2020. Study on decay characteristics of vertical four-vortex system for increasing airport capacity. Aerosp. Sci. Technol. 105, 106017.

Christiansen, I., 1973. Numerical simulation of hydrodynamics by the method of point vortices. J. Comput. Phys. 13 (3), 363–379.

Coletta, M., De Gregorio, F., Visingardi, A., Iuso, G., 2019. PIV data: Vortex detection and characterization.

Cone, C., 1962. The Theory of Induced Lift and Minimum Induced Drag of Nonplanar Lifting Systems. National Aeronautics and Space Administration.

Cornell Lab of Ornithology, 2019. Peregrine falcon. All About Birds URL: https://www.allaboutbirds.org/guide/Peregrine_Falcon/overview.

Heyes, A., Jones, R., Smith, D., 2004. Wandering of wing-tip vortices. In: Proceedings of the 12th International Symposium on Applications of Laser Techniques To Fluid Mechanics. pp. 35–3.

Hui, Z., Cheng, G., Chen, G., 2021. Experimental investigation on tip-vortex flow characteristics of novel bionic multi-tip winglet configurations. Phys. Fluids 33 (1), 011902.

Klei, C., Buffo, R., Stumpf, E., 2014. Effects of wing tip shaping on noise generation. In: INTER-NOISE and NOISE-CON Congress and Conference Proceedings. Vol. 249, Institute of Noise Control Engineering, pp. 1984–1993.

KleinHeerenbrink, M., Johansson, C., Hedenström, A., 2017. Multi-cored vortices support function of slotted wing tips of birds in gliding and flapping flight. J. R. Soc. Interface 14 (130), 20170099.

Leweke, T., Le Dizes, S., Williamson, C., 2016. Dynamics and instabilities of vortex pairs. Annu. Rev. Fluid Mech. 48, 507–541.

Liu, D., Cheng, J., Song, B., Yang, W., Xue, D., 2023. Numerical investigation of non-planarity and relative motion for bionic slotted wings. AIP Adv. 13 (8).

Liu, D., Song, B., Yang, W., Yang, X., Xue, D., Lang, X., 2021. A brief review on aerodynamic performance of wingtip slots and research prospect. J. Bionic Eng. 18, 1255–1279.

Lynch, M., Mandadzhiev, B., Wissa, A., 2018. Bioinspired wingtip devices: a pathway to improve aerodynamic performance during low Reynolds number flight. Bioinspir. Biomim. 13 (3), 036003.

Meunier, P., Ehrenstein, U., Leweke, T., Rossi, M., 2002. A merging criterion for two-dimensional co-rotating vortices. Phys. Fluids 14 (8), 2757–2766.

Midmer, A., Bruecker, C., 2022. Nature-inspired self-adaptive wingtip for vortex mitigation. In: RAeS Applied Aerodynamics Conference.

Newman, B., 1958. Soaring and gliding flight of the black vulture. J. Exp. Biol. 35 (2), 280–285.

Schmitz, A., Ponitz, B., Brücker, C., Schmitz, H., Herweg, J., Bleckmann, H., 2015. Morphological properties of the last primaries, the tail feathers, and the alulae of Acipiter nisus, Columba livia, Falco peregrinus, and Falco tinnunculus. J. Morphol. 276 (1), 33–46.

Servant, K., 2013. Barn owl flying. Wikimedia Commons URL: https://commons.wikimedia.org/wiki/File:Barn_Owl_flying.jpg.

Sharp, C., 2016. Turkey vulture (Cathartes aura aura) in flight, Vinales, Cuba. Wikimedia Commons URL: https://commons.wikimedia.org/wiki/File:Turkey_vulture_(Cathartes_aura)_in_flight.JPG.

Siddiqui, N., Aldeeb, M., Asrar, W., Sulaeman, E., 2018. Experimental investigation of a new spiral wingtip. Int. J. Aviat. Aeronaut. Aerosp. 5 (2), 6.

Song, J., Chen, W., Yan, D., Guo, S., 2021. Study on drag reduction of flexible structure under flows. In: E3S Web of Conferences. Vol. 245, EDP Sciences, p. 01019.

Tangermann, E., Ercolani, G., Klein, M., 2022. Aerodynamic behavior of a biomimetic wing in soaring flight–A numerical study. Flow Turbul. Combust. 109 (4), 1155–1173.

Thielicke, W., Stamhuis, E., 2014. Pivlab towards user-friendly, affordable and accurate digital particle image velocimetry in MATLAB. J. Open Res. Softw. 2 (1), e30. http://dx.doi.org/10.5334/jors.bl.

Tucker, V., 1993. Gliding birds: reduction of induced drag by wing tip slots between the primary feathers. J. Exp. Biol. 180 (1), 285–310.

Tucker, V., 1995. Drag reduction by wing tip slots in a gliding Harris' hawk, Parabuteo unicinctus. J. Exp. Biol. 198 (3), 775–781.

Williams, D., 2019. The Apollo 15 Hammer-Feather Drop. NASA, URL: https://nssdc.gsfc.nasa.gov/planetary/lunar/apollo_15_feather_drop.html.

Wissa, A., Han, A., Cutkosky, M., 2015. Wings of a feather stick together: morphing wings with barbule-inspired latching. In: Conference on Biomimetic and Biohybrid Systems. Springer, pp. 123–134.